Tomography of Materials and Structures 6 (2024) 100040

Contents lists available at ScienceDirect

Tomography of Materials and Structures

journal homepage: www.journals.elsevier.com/tomography-of-materials-and-structures

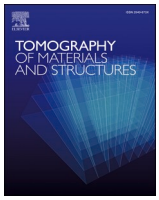

3D empirical mineral dissolution model of galena (PbS) in ethaline solution

Chandra Widyananda Winardhi [a,b,*], Jose Ricardo da Assuncao Godinho [b], Veerle Cnudde [a,c], Jens Gutzmer [b,d]

[a] PProGRess–UGCT, Department of Geology, Ghent University, Ghent 9000, Belgium
[b] Helmholtz-Zentrum Dresden-Rossendorf, Helmholtz Institute Freiberg for Resource Technology, Freiberg, Germany
[c] Environmental Hydrogeology, Department of Earth Sciences, Utrecht University, Utrecht, CS 3585, the Netherlands
[d] PPM Group, Department of Geology, University of Johannesburg, South Africa

ARTICLE INFO

Keywords:
Computed tomography (CT)
Macroscopic features
Mineral dissolution
Mineral geometry
Empirical dissolution model

ABSTRACT

Mineral dissolution is an important process that occurs in both natural as well as anthropogenic processes. The kinetics of such dissolution processes are influenced not only by the characteristics of the solution but also by the characteristics of the minerals, such as crystal defects on the microscopic scale or macroscopic features such as the intersection of crystal planes to form edges and corners. Macroscopic features are known to increase the population of steps and kinks that may, in turn, affect the dissolution rate over time. Hence, this study presents a 3D empirical dissolution model aimed at examining the time-series evolution of macroscopic features together with the corresponding changes in the dissolution rate under far from equilibrium batch reactor conditions. The developed empirical model is based on the mineral geometry (surface topography and volume) derived from X-ray computed tomography (CT) measurements. The macroscopic features are identified using surface curvature which are then used to generate reactivity maps for dissolution model. As a study case, the dissolution of monomineralic galena (PbS) in ethaline and iodine as oxidizing agent is experimentally observed and then modelled. The model is then applied to seven particles of various shapes and sizes. The finding suggests that the surface reactivity increases over time as the particle shrinks and the macroscale steps and edges become dominant over the initial terraces. This implies that the persistent highly reactive surface sites defined by a particle's geometry may play a dominant role in the overall particle dissolution in addition to the dissolution mechanisms typically studied on near atomic-flat surfaces. The model developed in this investigation offers the opportunity to be extended providing the possibility of simulating the dissolution of multi-mineral particles during batch dissolution experiments.

1. Introduction

Mineral dissolution has been intensively investigated as it is an important process that occurs both in nature (e.g. groundwater [18,44] or seawater [48]) as well as in technical processes including CO_2 sequestration [8,33], hydrogen storage [2,20] and metal extraction [1]. For instance, tank leaching is an important metal extraction method [34] that involves agitating the ores in a stirred reactor with a leaching solution to induce the dissolution of the valuable minerals. The investigation of mineral dissolution processes typically involves measuring the concentration of dissolved elements of interest within the leaching solution. Information about the solids or mineral assemblages (e.g. mineral association, reactive surface area) during the dissolution processes is, in contrast, usually ignored. This is based on the assumption that the variability caused by individual particle properties average out across many particles that are exposed to dissolution. Furthermore, it has recently been shown that different mineral assemblages lead to significantly different results during dissolution experiment [50] as the surface evolves throughout the dissolution process.

To monitor the dissolution of minerals more accurately, 3D surface measurements like vertical scanning interferometry (VSI) [22] and atomic force microscopy (AFM) [41] and 3D volume measurements using X-ray computed tomography (CT) can be used [16,22]. However, while 3D surface measurements provide nanometer resolution, they often require near-flat surfaces and are limited to small regions on a single plane. This limitation prevents the possibility of providing information on the entire particle geometry towards dissolution. To complement those studies, CT measurements are non-destructive [7,51]

* Corresponding author at: PProGRess–UGCT, Department of Geology, Ghent University, Ghent 9000, Belgium.
E-mail address: chandra.winardhi@ugent.be (C.W. Winardhi).

https://doi.org/10.1016/j.tmater.2024.100040
Received 20 March 2024; Received in revised form 7 June 2024; Accepted 11 July 2024
Available online 13 July 2024
2949-673X/© 2024 The Author(s). Published by Elsevier B.V. This is an open access article under the CC BY license (http://creativecommons.org/licenses/by/4.0/).

and capable of resolving the entire particle geometry along with their macro features with micrometer resolution. CT allows the observation of the development of entire particle surfaces and geometry throughout dissolution processes [35], thus providing a complete view of the dissolution dynamics. From such studies it is widely understood that the dissolution rates cannot be represented by a constant value, but rather by a distribution of values across the mineral surface. Such distributions are referred to as dissolution rates spectra or local dissolution rates [9,29]. Using AFM or VSI, the dissolution rates spectra are known to be influenced by the morphology of the mineral grain surface as well as surface defects such as etching and pitting [17]. The latter act as source for the dissolution process that then propagates as step-waves [28]. In investigations at a larger scale, such as millimeter scales using CT, it has been shown that intersections of two or more crystal planes (corners and edges, macroscopic features) play a significant role during dissolution [16,36,53]; it increases the population of steps and kinks over time, which also affects the surface surrounding the macroscopic features [49].

In order to understand the development of surface features in greater detail, modelling approaches such as kinetic Monte-Carlo (kMC) simulations [25,27] are often applied. Coupled with 3D surface measurements kMC simulations can provide geometry information and can estimate the probability of a neighboring atom being released from the mineral surface. This approach offers high accuracy in simulating mineral dissolution. Yet, Monte-Carlo simulations that consider larger surface areas (e.g. at millimeter scale) remain challenging as they are computationally demanding [19,31]. Therefore, other modelling approaches such as the shrinking core model (SCM) [52] and particle-based simulations [50] were introduced to simulate mineral dissolution. SCM is not only known for its thermodynamic accuracy, but it also has the advantage of permitting simulation at a larger scale, including batch leaching simulation. However, the SCM assumes the dissolving particle to be spherical and ignores associated minerals. On the other hand, particle-based simulation uses a combination of calculated global bulk dissolution rates (normalization of dissolution rates by the total surface area of the dissolving minerals) derived from 3D volume measurements with classified mineral maps obtained by SEM-based image analysis methods [45]. Despite providing modal mineralogy and mineral assemblage data, this approach currently is limited to 2D data and assumes that all surfaces of the mineral dissolve in a similar manner by utilizing global bulk dissolution rates. The actual geometry of mineral grains and particles is not considered. Ghorbani et al. [12] and Lin et al. [30] proposed a 3D heap leaching dissolution model that incorporated the particle geometry and used CT results as the model inputs. Both showed that the simulated particle leaching behavior did not follow the predicted result from SCM. However, both were done on column dissolution experiments, in which dissolution might be affected by the flow inside the column. Additionally, both models required the need to solve the mass transport equation on the 3D particles, an approach that is computationally intensive.

This research introduces a 3D empirical dissolution model in an attempt to investigate the dissolution behavior of mineral grains and particles with different geometries during a dissolution process. We hypothesize that the evolution of macroscopic features will affect the dissolution rate spectra and that this will impact the dissolution behavior depending on the initial geometry of the particle. As a study case, a cubic monomineralic lead-sulfide (PbS, galena) was dissolved in ethaline. Ethaline is a deep eutectic solvent (DES) that is biodegradable [38] and has a low melting point; it is similar to other DES often regarded as a "green" solvents [23,37]. The ethaline solution dissolves galena faster than other sulfides, such as pyrite or chalcopyrite [6,50], which makes it a promising solvent to recover trace metals such as bismuth (Bi), tellurium (Te) and silver (Ag) [11,32] commonly present in galena. The results of the 3D geometrical evolution of the dissolving galena particle measured by CT are presented.

Based on this experimental result, a 3D empirical dissolution model was developed and applied to a set of galena particles by calculating reactivity maps from the initial geometry of each particle as proposed by Winardhi et al. [49]. The reactivity maps were generated by correlating dissolution rates spectra obtained from experimental result with the calculated distance between the mineral surface (surface points) towards macroscopic features (features points). As an attempt to apply the algorithm to various particles, these macroscopic features were classified by computing surface curvatures derived from the initial geometry of the dissolving particle. This approach provides not only the information on the initial reactivity of a particle geometry, but also the mineral particles dissolution behavior over time. Furthermore, this approach can be applied to any particle regardless of its size and geometry; it could thus benefit the optimization of dissolution processes.

2. Materials and methods

2.1. Materials

Monomineralic galena (PbS) particles originated from Freiberg, Germany and provided by Geoscientific Collection of the TU Bergakademie Freiberg were investigated in this study. The galena was chosen due to its simple chemical composition and cubic crystal structure. Two sets of galena samples were prepared: a single galena particle (referred to as "galena-x") and another set consists of seven galena particles (particle-1, particle-2, particle-3, particle-4, particle-5, particle-6 and particle-7) with various shapes and sizes (referred to as "the seven galena particles"). The dissolution behavior of the galena-x particle has already been described in details by Winardhi et al. [49], while the seven further galena particles analyzed as part of this study. The galena-x particle is used to provide proof of concept to test the 3D empirical dissolution model that is developed in this study. The simulation results are then compared with the results obtained from the dissolution experiment.

The seven galena particles serve to test the hypothesis that the dissolution process over time can be simulated using the particles initial geometry and the dissolution rates specific to its macroscopic features. The seven galena particles were prepared using the method proposed by Godinho et al. [15] to reduce artifacts and further enhance the segmentation process. Altogether, the seven galena particles weighed 0.015 g their particle size ranged from 120 – 170 μm. These were mixed with 0.55 g sugar crystals ranging in size between 107 μm and 315 μm that, acted as a spacer. Epoxy was added to this mixture and cast on a 6 mm inner diameter tube with length of 2 cm resulting a cylindrical sample with 5 mm diameter and 1.5 cm length. This sample contained the seven galena particles.

2.2. Dissolution experiments

Prior to dissolution, one cleavage surface of the galena-x particle was covered with epoxy resin. This surface acts as a reference for the registration process of the CT images while, the other surfaces were exposed to react with DES solvent, ethaline. The ethaline solution was prepared by mixing a 1:2 M ratio of choline chloride (ChCl, Sigma Aldrich, >98 %) and ethylene glycol (EG, Merck, >98 %) with the addition of 100 mM iodine (I_2) as an oxidizing agent [21]. The solvent was stirred at 500 rpm in a closed container at 50 °C until a homogeneous solution was obtained. The dissolution experiment was done by adapting the single particle leaching method by Winardhi et al. [50]. This method allows the particle to move freely within a stirred beaker filled with ethaline solution, thereby minimizing the variations due to other experimental factors (e.g. interaction between particles in solution, heterogeneous movement of fluid around the particle, temperature, pressure, fluid composition and concentration gradients) (Fig. 1). It was assumed that the system remained far from equilibrium and that all surface points on the particle were equally exposed to dissolution, therefore isolating the effect of macroscopic features as the only source for the variability of

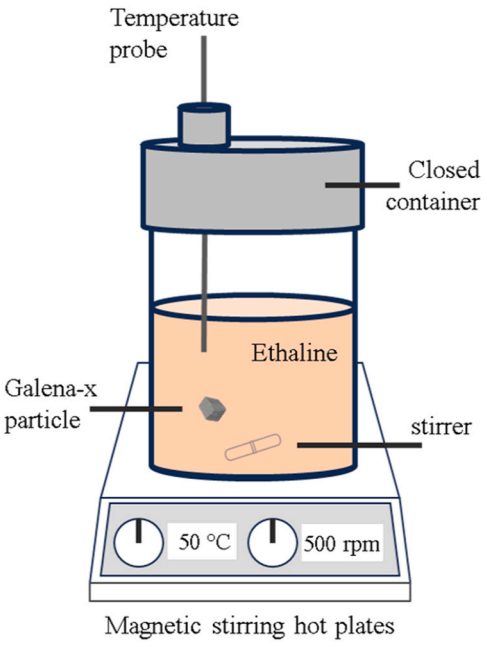

Fig. 1. Experimental setup of the single particle leaching experiment adapted from Winardhi et al. [49]. The galena-x particle was reacted with ethaline solution in a closed container at constant 50 °C and 500 rpm.

dissolution rates across the various particle surfaces. The galena-x particle was scanned by CT prior to the onset of the dissolution experiment. The galena-x particle was exposed to the ethaline solution at atmospheric pressure for 8 h with an agitation rate of 500 rpm and a constant temperature of 50 °C. After the dissolution experiment, the galena-x particle was recovered and rinsed with ethylene glycol to prevent precipitation of lead(II) chloride [46], followed by ethanol to remove the residues of ethaline. It was then scanned again by CT to acquire the 3D volume after dissolution.

2.3. X-ray computed tomography (CT)

Both samples (galena-x particle and the seven galena particles) were scanned using a TESCAN XRE CoreTOM CT instrument located at the Helmholtz Institute Freiberg for Resource Technology. Scanning was done at a voxel size of 4.65 μm, 180 kV accelerating voltage, 15 W power, 1500 ms exposure time, and a 50 μm thick tungsten sheet mounted at the source to filter the X-ray beam. Acquila 1.0.0.70 reconstruction software (TESCAN) was used to reconstruct the radiographs. Image processing of the reconstructed images was conducted using the Avizo 9.2.0 software package. All reconstructed images were filtered using a non-local means filter [10] to reduce the noise and maintain the quality of the particle surface. Before the calculation of dissolution rates, the dissolved galena-x particle was registered to the initial condition prior to dissolution using an image registration module in Avizo. The registration module utilizes a rigid transformation and a normalized mutual information metric [47]. Two optimization algorithms within the registration module were applied: (i) extensive-direction optimization for coarse optimization with a final convergency value of 0.16 and (ii) finer optimization using a quasi-newton algorithm with a final convergency value of 0.1. After the registration, the 3D volume was transformed to the registered coordinate by applying the resample transform image module with Lanczos interpolation [5]. Segmentation was then carried out using the region-growing algorithm with an initial masking grey-value of 25, 000–65,535 [42].

The 3D segmented data allows the possibility to calculate global bulk dissolution rates (k_i, $\mu m.h^{-1}$) and normalized bulk dissolution rates (k_{norm_i}, $mol.m^{-2}.s^{-1}$). The global bulk dissolution rates (k_i) was calculated using the difference of the segmented particle volume before (V_{t_0}) and after a dissolution stage (V_{t_i}) with a given time interval ($t_i - t_0$). This rate is normalized to the average surface area ($\overline{A_{t_0,t_i}}$) between two-time steps t_i and t_0 (Eq. (1)), [14]. The normalized bulk dissolution rates (k_{norm_i}) was obtained by using the global bulk dissolution rate (k_i) normalized with the molar volume of galena ($\upsilon_{gal} = 3.03 \times 10^{-5}$ $m^3.mol^{-1}$) (Eq. (2), [36].

$$k_i = \left(\frac{V_{t_0} - V_{t_i}}{t_i - t_0}\right).\frac{1}{\overline{A_{t_0,t_i}}} \tag{1}$$

and

$$k_{norm_i} = \frac{k_i}{\upsilon_{gal}} \tag{2}$$

The uncertainty of the global bulk dissolution rate due to segmentation was assumed to be two voxels layer of the surface calculated by applying a one-voxel distance dilation or erosion with 6-connectivity from the segmented particle.

The dissolution rates spectra was calculated based on the surface retreat between two adjacent time steps as proposed by Noiriel et al. [36]. A chamfer distance map [3] was computed for the segmented particle prior dissolution, providing distance values perpendicular from the nearest surface within each voxel towards the center of the particle. Then, by using the segmented surface of the particle after dissolution as a mask, the dissolution rates spectra over the particle surface were obtained. Possible uncertainty of the calculated dissolution rates spectra due to misregistration was calculated by applying the method proposed by Noiriel et al. [36]. A new volume was generated by applying 5-voxel erosion with 18-connectivity. Then, (i) a 2-pixel horizontal shift and (ii) a 1° vertical tilt angle were applied. The dissolution rates spectra of the new volumes (eroded, shift and tilt) were then computed using the same method.

2.4. Empirical dissolution model

The workflow of the empirical dissolution model is illustrated in Fig. 2 and was developed using MATLAB MathWorks. Based on the single particle leaching method described in the experimental section, the empirical dissolution model assumes that other variables affecting the dissolution kinetics remain approximately constant. Thus, only the macroscopic features of the particle influence the rate spectra and, since every particle has a unique geometry, the variability of the overall dissolution rate for different particles. In order to detect the macroscopic features, the model utilizes surface curvature calculations of the segmented particle as input. This allows the model to detect the evolution of macroscopic features and particle geometry for every iteration of dissolution simulation, also providing information about the local and overall dissolution rates over the course of the dissolution of the entire particle. The proposed empirical dissolution model employs the reactivity map calculation proposed by Winardhi et al. [49]. In order to generate the reactivity map, the macroscopic features of the particle need to be defined. Winardhi et al. [49] defined these macroscopic features manually based on user input. In dissolution simulation, the manual selection of macroscopic features is overwhelmingly time-consuming since due to the evolving geometry the procedure must be repeated for each iteration step. This requirement becomes even more challenging when multiple particles are considered.

To solve this challenge, an automated approach was applied in this study to define the macroscopic features of the particle at each iteration. In this approach, the Gaussian curvatures of the particle surface [24] were computed by applying a 3x3x3 kernel operation. This kernel moves over the particle surface and calculates the second-order derivatives in all directions (x, y and z), resulting in a gradient matrix of the particle surface. This gradient matrix represents the surface characteristic of the

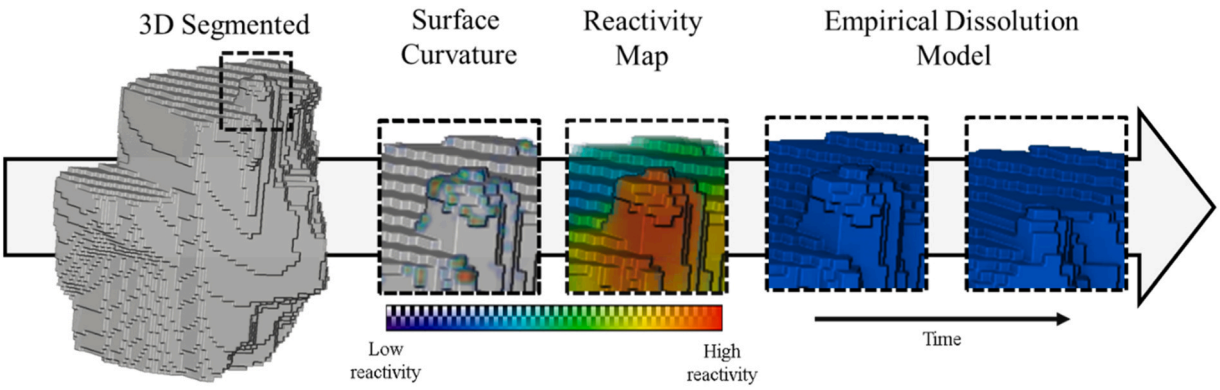

Fig. 2. A simplified illustration of the workflow associated with the 3D empirical dissolution model, starting with the 3D segmented particle. Surface curvature was computed using the segmented particle to generate the reactivity map, which is used as initial input for the empirical dissolution model.

mineral [54]. By calculating the eigenvalues of this gradient matrix, the first and second principal curvature are obtained. The multiplication product of these principal curvatures results in the Gaussian curvature. The Gaussian curvature has both positive and negative values, in which positive values show outward-facing features (e.g. convex corners or edges), while negative values show inward-facing features (e.g. re-entrant corners or edges). In this study, it was assumed that the inward-facing features (voxels with negative Gaussian curvature values) would have a relatively small dissolution rate. Hence, the negative curvature values are reset to 0. Additionally, based on the curvature values, features to surface area percentage (FSP) can be calculated. The FSP represents the detected macroscopic features coverage percentage over the particle surface, thus it is defined as the amount of surface voxels with curvature values bigger than 0 ($N_{curvature>0}$) and divided by the surface area (A) of the particle (3)).

$$FSP = \frac{N_{curvature>0}}{A} \times 100\% \quad (3)$$

The curvature values obtained from the Gaussian curvature calculation were assumed to be the macroscopic features of the particle surface (so-called feature points). In order to generate the reactivity map, all voxels that have curvature values equal to zero were defined as surface points. Then, the distances between these surface points and all feature points were calculated as vectors to obtain the position of both surface and features points within the 3D particle volume. By correlating the distance map and the dissolution rates spectra obtained from the dissolution experiment [49], the exponential constants (− b) for each curvature value was obtained by using exponential fitting (4), where the dissolution rate (k) at a surface point decreases with the distance from a macroscopic features (d_f). The constant c and a can be interpreted as the minimum and maximum dissolution rate correlated to a specific macroscopic feature.

$$k(d_f) = a.\exp^{-b.d_f} + c \quad (4)$$

As the macroscopic features surrounding a surface point affect the cumulative reactivity of that surface point [49], the reactivity map ($R_{f_{ij}}$) then was calculated by using the sum of the exponential parts of each curvature value (− b_i) derived from Eq. (4) and the distance between the surface points towards all feature points (d_{fj}) as shown in Eq. (5).

$$R_{f_{ij}} = \sum_{i=1}^{n} \sum_{j=1}^{m} \exp^{-b_i.d_{f_j}} \quad (5)$$

After generating the reactivity map, the 3D empirical dissolution model can be computed. Initially, from the 3D segmented volume, the neighborhood of each voxel was calculated into six directions (up, down, left, right, front and back). Voxels with less than six neighborhoods were labelled as surface, while the voxel with six neighborhoods was labelled as volume. Given that the calculated reactivity map is closely linked to the dissolution rate spectra (4), it was assumed that reactivity is best expressed as $\mu m.h^{-1}$. Therefore, the reactivity values were used as a condition to remove a voxel from the 3D volume during the dissolution simulation. Based on the calculated neighborhood value of each voxel, the removal process will only remove the voxels if it was labelled as surface. Each time one or more voxels were removed from the particle surface during the simulation, the particle volume was updated and the neighborhood was recalculated to determine the new surface. Then, the reactivity map was recalculated by recomputing the Gaussian curvature and the distance map. The iteration time steps (d_t) were chosen based on the highest reactivity value obtained from the reactivity map. This is best illustrated by an example: The highest reactivity value calculated for the initial galena-x particle was 18 $\mu m.h^{-1}$. This suggests that 0.055 h (or 198 s) are needed to dissolve 1 μm of galena from this surface feature. Accordingly, iteration time steps (d_t) of 0.001 h (3.6 s) were chosen for the dissolution model.

Within this study, the simulation of the galena-x was stopped when the iteration time reached the same amount of time as the experiment (8 h). Different conditions were applied to the simulation of the dissolution of the seven galena particles. First, the seven galena particle dissolution simulation used the exponential constant (Eq. (5)) obtained from galena-x particle to generate the reactivity map. Second, due to the kernel size used during the calculation of the Gaussian surface curvature being 3x3x3 voxels, the minimum voxel needed to distinguish between terraces and the macroscopic features, was assumed to be 4^3 voxels. Thus, the simulation for the seven galena particles continued until the simulated particle size reached less than 64 voxels (equal to 6.43×10^3 μm^3). The empirical dissolution models for both galena-x particle and the seven galena particles were computed on a workstation equipped with the 13th generation Intel i9 processor utilizing parallel processing across 24 cores and 128 GB of random-access memory (RAM).

3. Results

This section starts with the comparison between the experimentally observed and simulated dissolution of the galena-x particle. This is followed by the empirical dissolution model applied to the seven galena particles, focusing on differences between the individual particles. This analysis includes the change of volume, reactivity and the evolution of global bulk dissolution rates over time.

3.1. Galena-x particle

The dissolution experiment conducted with the galena-x particle shows a distinct decrement in volume and surface area within 8 h of dissolution (Table 1). The calculated global bulk dissolution rate and normalized dissolution rate was 0.99 $\mu m.h^{-1}$ and 9.15×10^{-6} $mol.m^{-2}$.

Table 1
Experimental and simulated data for the surface area, volume and its calculated normalized dissolution rate of the galena-x particle, along with the upper and lower limit calculation based on dilation and erosion of the segmented particle.

	Time (h)	Surface area (μm^2)	ε_{SA} (%)	Volume (μm^3)	ε_{Vol} (%)	k_i ($\mu m.h^{-1}$)	k_{norm_i} ($mol.m^{-2}.s^{-1}$)	ε_{knorm} (%)
Experiment	0	2.15×10^6	2.46	2.27×10^8	4.57	-	-	
	8	1.98×10^6	2.35	2.10×10^8	4.46	0.99	9.15×10^{-6}	3.81
Simulated	8	1.94×10^6	1.90	2.09×10^8	0.63	1.09	9.98×10^{-6}	10.1

* Represents the maximum errors calculated from the one-voxel distance dilation and erosion of the segmented particle.

s^{-1} respectively. The calculated uncertainty derived from a one-voxel erosion and dilation with 6-connectivity, resulted in a maximum surface area (ε_{SA}) and volume variation (ε_{Vol}) of 2 % and 5 % respectively. Consequently, the upper limit (dilated) and the lower limit (eroded) of the experimental global bulk dissolution rate were 1.03 $\mu m.h^{-1}$ and 0.96 $\mu m.h^{-1}$ respectively, resulting in a maximum uncertainty (ε_{knorm}) of 4 % on the dissolution rate (Table 1).

The dissolution rate is, however, not equal throughout the surface. Thus, the bulk dissolution rate cannot be applied to particle dissolution models as this would result in homogeneous retreat over the particle surface, neglecting the effect of macroscopic features on dissolution. The visualization of the dissolving galena-x particle (Fig. 3) illustrates the different behavior of macroscopic features during the dissolution process. The distinct evolution of the particle corners becomes rounded due to dissolution, as displayed in the 2D ortho-slice (black arrow, Fig. 3a and b). The edges become more evident within the 3D volume (blue arrow, Fig. 3a and b), suggesting that dissolution occurs more rapidly at these macroscopic features. This becomes more apparent in the calculated surface retreat, namely dissolution rate spectra (Fig. 3c), where dissolution is higher on these macroscopic features (red-yellow color). On the other hand, the particle terraces appear to be dominated by white and light purple color, indicating substantial heterogeneity within the dissolution process. The heterogeneity further demonstrates that dissolution rates decrease as the distance from macroscopic features increases.

Additionally, the uncertainty of the dissolution rates spectra can be calculated based on the assumption of homogeneous dissolution rates over the surface. With a global bulk dissolution rate of 0.99 $\mu m.h^{-1}$ observed in the experiment, a surface retreat of 7.9 μm was expected after 8 h of dissolution. The voxel resolution of 4.65 $\mu m.px^{-1}$ translates to an expected surface retreat of 1.7 pixels. An uncertainty of ±1 pixel (equivalent to ±2 $\mu m.h^{-1}$) is assumed [49]. Thus, all points of the surface with dissolution below 2 $\mu m.h^{-1}$ were considered below the detection limit and were not accounted for in the later empirical dissolution model. Meanwhile, the possible uncertainty due to misregistration resulted in the average surface retreat and standard deviation of the eroded, shifted and tilted resulted in 5.61 ± 1.05, 5.60 ± 1.22 and 5.67 ± 1.62 pixels, respectively (comparison of the calculated surface retreat distribution between eroded, shifted and tilted can be found in Appendix A, Figure A.1). This result shows that misregistration did not significantly affect the average surface retreat but increased the standard deviation which may affect the calculated dissolution rates spectra.

The reactivity map derived from the initial condition of galena-x particle displays surface heterogeneity of reactivity due to macroscopic features (Fig. 3d). The reactivity map effectively captures the influences of the macroscopic features toward the neighboring surfaces: corners appear red color, edges display yellow to green color and terraces show a light purple color. The reactivity map correlates well with the dissolution rates spectra, with high reactivity indicated by the white arrow corresponding to high dissolution rates within the dissolution

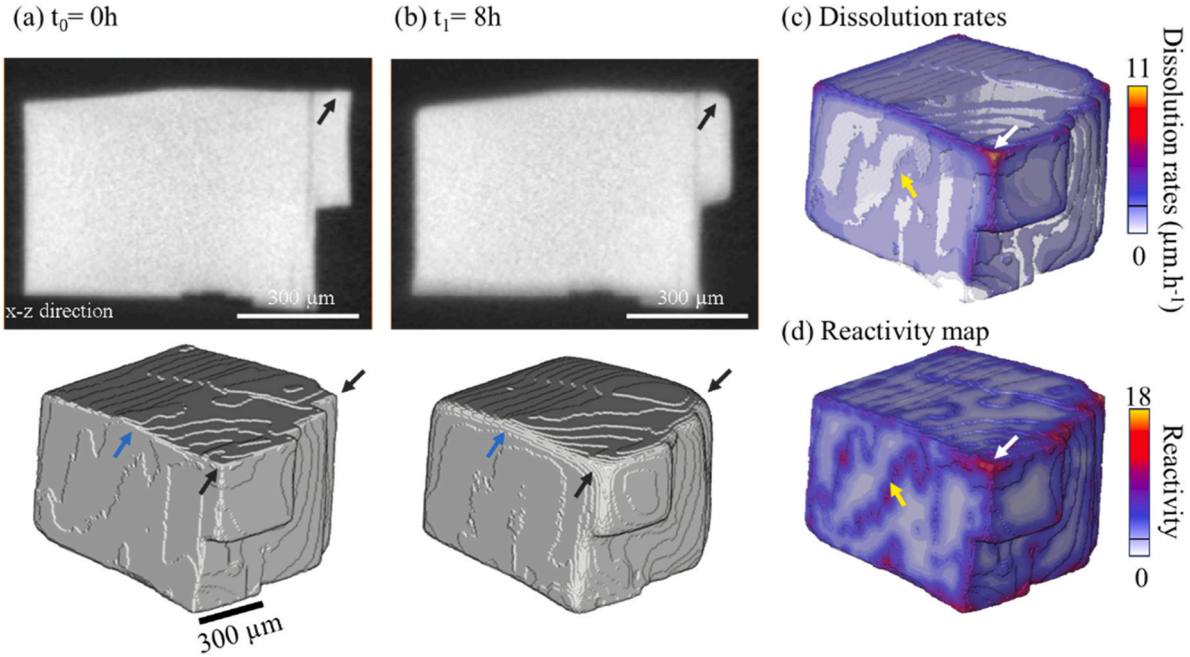

Fig. 3. Dissolution experiment of galena-x particle adapted from [49], ortho-slice in x-z direction and binary 3D volume of (a) prior to the dissolution experiment, (b) after 8 hours of dissolution (c) the calculated dissolution rates spectra over the particle surface and (d) the calculated reactivity map. Notice the black arrows indicating the rounding of the macroscopic feature due to dissolution, while the white arrow and yellow arrow highlights the similarity and the marked difference between the dissolution rates spectra and the reactivity map, respectively. The white and light blue colour (marked in with a line in the scalebar) represent dissolution rate values below the uncertainty of ±2 $\mu m.h^{-1}$.

rates spectra. However, some steps within the particle terraces (pointed by yellow arrows) exhibit high reactivity despite corresponding to low dissolution rates. To simulate the observed enhanced dissolution at macroscopic geometric features an empirical model was developed by utilizing the reactivity map which was based on the initial geometry of a particle. The simulation of 8 h of dissolution of the galena-x particle, with a total initial volume of 2252,821 voxels, required approximately 6.7 h of computing time. The empirical models also allowed the calculation of FSP, which shows 36 % of the galena-x surfaces are considered macroscopic features and the remaining 64 % as terraces with much a dissolution rate below the detection limit of this study. However, the empirical dissolution model presents simulated surface area and volume smaller than the experimental result, which results in simulated global bulk dissolution rates 9 % higher than the experimental result (Table 1). This discrepancy between experimental and simulated results is tentatively attributed to the uncertainties of dissolution rates occurring within the particle terraces.

3.2. Seven galena particles

The ortho-slice in the y-z direction of the seven galena particles (particle 3, 4, 6 and 7, provided in Appendix A, Figure A.2) demonstrated that CT was able to distinguish the macroscopic features, such as convex corner and the re-entrant corner. Despite the streak artefact caused by the sharp corner of the galena particles, the image quality was sufficient to segment the galena particles from the background and the artefacts. Additionally, the sample preparation method proposed by Godinho et al. [15], showed that the artefacts did not significantly affect the grey-scale distribution within particles, thereby enhancing the segmentation process.

Based on the results obtained for the galena-x particle, the applied model utilizes the segmented image of the seven galena particles as input to generate the reactivity map of all seven particles (Fig. 4). Initially, all particles have different shapes and sizes, thus have a different distribution of macroscopic features. For example, particle-1 and particle-7, show small surface protrusions (red arrow), while others, including particle-5 and particle-6, are marked by the presence of larger terraces (blue arrow). The protrusions are most apparent within the calculated reactivity map, clearly suggesting a high reactivity. Terraces in contrast, are not marked by increased reactivity values. On the contrary, the reactivity map is also able to identify surfaces, such as terraces, that exhibit staircase morphology (blue arrow). It was also evident that the calculated FSP of the particles corresponds to the total dissolution time required, with smaller FSP leading to less reactivity and longer dissolution time required to dissolve the particles.

The computing time for all seven galena particles with an average of 139,145 voxels took around 5 h to simulate an average of 38 h of dissolution time. The calculated particles initial volume, FSP and calculated average reactivity are presented in Table 2. The average reactivity values were calculated by summing all reactivity values over the surface and normalizing them with the total surface area. These average reactivity values belong to the initial particle condition prior to the dissolution simulation. In general, the presented particle characteristics are consistent with one another. As an example, particle-1 dissolves the fastest in comparison to the other particles. Particle-1 almost completely dissolves after 26 h while the other requires more than 30 h for dissolution. Although particle-1 is also the smallest particle, it displays a high FSP of 29.23 %, resulting in high reactivity. Similar to particle-1, particles-4 and 7 exhibit the same behavior, where their total

Table 2
Summary of measured and simulated properties for the seven galena particles sorted in order of increasing initial Features to Surface Percentage (FSP), including initial volume, Feature to Surface Percentage (FSP), average reactivity and the total estimated time required to dissolve the particles.

S	Volume (μm^3)	FSP (%) *	Average reactivity **	Total dissolution time (h)
1	0.89×10^7	29.23	1.33	26.08
7	0.99×10^7	24.87	1.09	32.97
4	1.11×10^7	20.53	0.98	35.01
2	1.47×10^7	18.52	0.73	35.64
3	1.68×10^7	18.00	0.88	36.19
6	1.74×10^7	17.26	0.68	39.3
5	1.91×10^7	17.14	0.69	38.72

* The FSP was calculated based on the surface voxels that has curvature value bigger than 0 and divided by the total surface voxels of the particles
** Values were calculated based on the reactivity map of the particle prior to the application of the empirical dissolution model

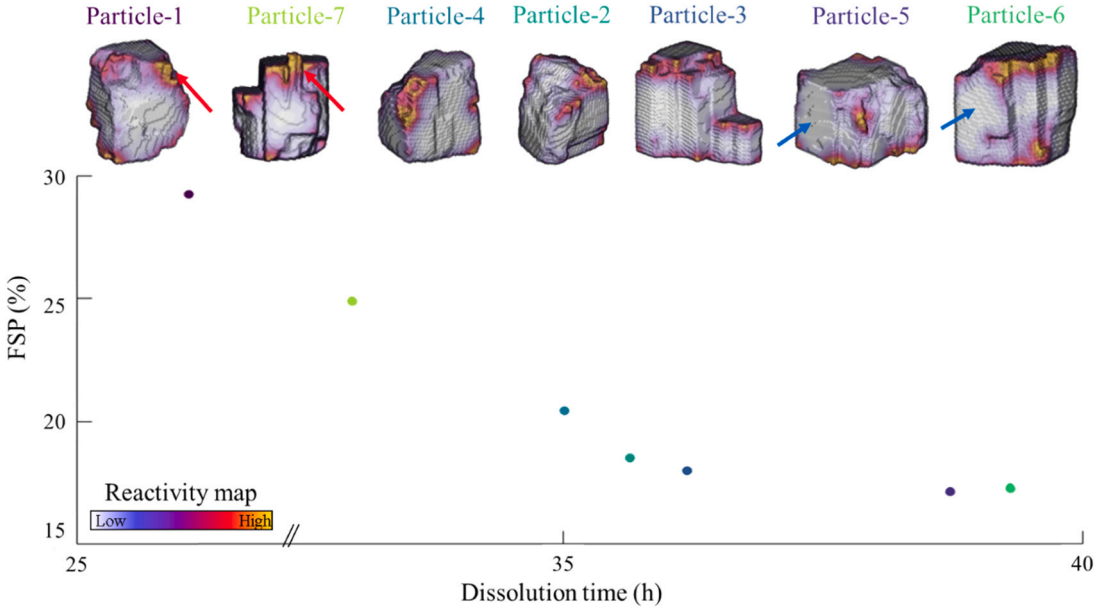

Fig. 4. Visualization of the seven galena particles calculated reactivity map, plotted based on their initial Feature to Surface Percentage (FSP) as a function of dissolution time needed to dissolve the particles completely. (Warm colors (red and yellow) denotes high reactivity while cold colors (blue-white) denote low reactivity (white represents below the detection limit).

dissolution time corresponds to their FSP and average reactivity values.

The particle volume is inversely proportional to the FSP, although this is not always proportional to the reactivity. Interesting results emerge when comparing particle-2 to particle-3 and particle-5 to particle-6. Although particle-3 exhibits a lower FSP compared to particle-2, it demonstrates a higher average reactivity value. In Fig. 4, while particle-2 displays a rough surface texture, particle-3 exhibits distinct corners and edges, which detected by the curvature algorithm as a macroscopic features, thus resulting in higher reactivity value (Fig. 4). Further investigation is presented in Fig. 5, showing the evolution of volume, global bulk dissolution rates and reactivity. During the first 10 h of dissolution simulation (Fig. 5a), it was evident that the difference between both particle volume evolution was reduced, suggesting an increase of particle-3 dissolution rates. This corresponds to the global bulk dissolution rate plot (Fig. 5b), which shows a larger increase in dissolution rates of particle-3 compared to particle-2. However, after 5 h of dissolution, particle-3 displayed the rates reaching a plateau that increases slightly over time, while particle-2 demonstrates a linear increase in dissolution rates. This behavior is also reflected in the reactivity plot (Fig. 5c), where both particles show an increase of reactivity over time. However, particle-2 displays a larger increment in reactivity after the first 10 hours.

On the other hand, both particle-5 and particle-6 display similar values of FSP and average reactivity. However, particle-6 requires only one additional hour to dissolve the particle completely in comparison to particle-5, despite having smaller size. Fig. 5 illustrates the decrease in volume of both particles through time. Similar to the comparison between particle-2 and particle-3, the difference between particle-5 and particle-6 becomes smaller over time, overlapping after 20 h of dissolution, suggesting an increasing dissolution rate for particle-5. This corresponds to the dissolution rates presented in Fig. 5e, both particles start with similar value, however particle-5 bulk rates increment was bigger than particle-6. The reactivity plot (Fig. 5f), within the first 5 h, particle-5 display a higher reactivity increment than particle-6, resulting in faster dissolution of particle-5 although having bigger volume. Visualization of particle-2, particle-3, particle-5 and particle-6 reactivity evolution along with the calculated FSP through the empirical dissolution simulation were presented in Fig. 6.

Prior to dissolution, all particles (particle-2, particle-3, particle-5 and particle-6) display high reactivity on corners and distinct edges of the particles (visualized as warm colors in Fig. 6). As dissolution time progresses, it becomes evident that all particles become distinctly rounded, which causes the number of detected features (FSP) to increase and resulted in an increase of the surface reactivity. Prior to dissolution, as illustrated in Fig. 6b, particle-2 presents a higher FSP, while particle-3 demonstrates higher reactivity. At viewing angles of 0° and 90° prior to dissolution, particle-3 displays significant reactivity on the sharp corners of the particle. After 5 h of dissolution, these corners start to disappear, leading to a decrease in reactivity within the region surrounding the corners. This was also displayed within Fig. 5b and c showing the curve reaching a plateau that slightly increases over time. Then, at 10 h of dissolution, particle-2 displays a higher calculated FSP value compared to particle-3, which corresponds to the dissolution rates and reactivity evolution presented in Fig. 5e and f. Meanwhile, particle-5 and particle-6 initially exhibit similar reactivity. After 5 h of dissolution, it is evident that particle-5 surfaces become more reactive from all viewing angles in comparison to particle-6. This is further supported by a higher FSP value calculated for particle-5 compared to particle-6 after 5 h of dissolution. This trend continues over time, leading to faster dissolution of particle-5 in comparison to particle-6.

4. Discussion

The calculated bulk dissolution rate of galena in ethaline solution is 0.99 $\mu m.h^{-1}$ with a maximum variation of 4 %. The calculated dissolution rate was consistent with the experiment done in a previous study [50], which observed dissolution rates of 1.81 $\mu m.h^{-1}$. In comparison with Winardhi et al. [50], the discrepancy could originate from one cleavage of the galena-x particle being masked with epoxy, thus resulting in fewer active edges and corners, which ultimately reduces the dissolution rate.

The proposed 3D empirical dissolution model is capable of tracking the geometric changes of mineral particles during the dissolution process. The simulation results show that all simulated particles become rounded as they decrease in size. This is consistent with observations from previous studies [49,50] as well as other literatures, both experimental [4,36,53] and numerical (Luttge et al., 2013; [16]). Furthermore, it is remarkable that this study yields dissolution rates for galena in ethaline solution (with iodine as an oxidizing agent) rather similar to those reported by Jenkin et al. [21]. The latter authors reported a galena

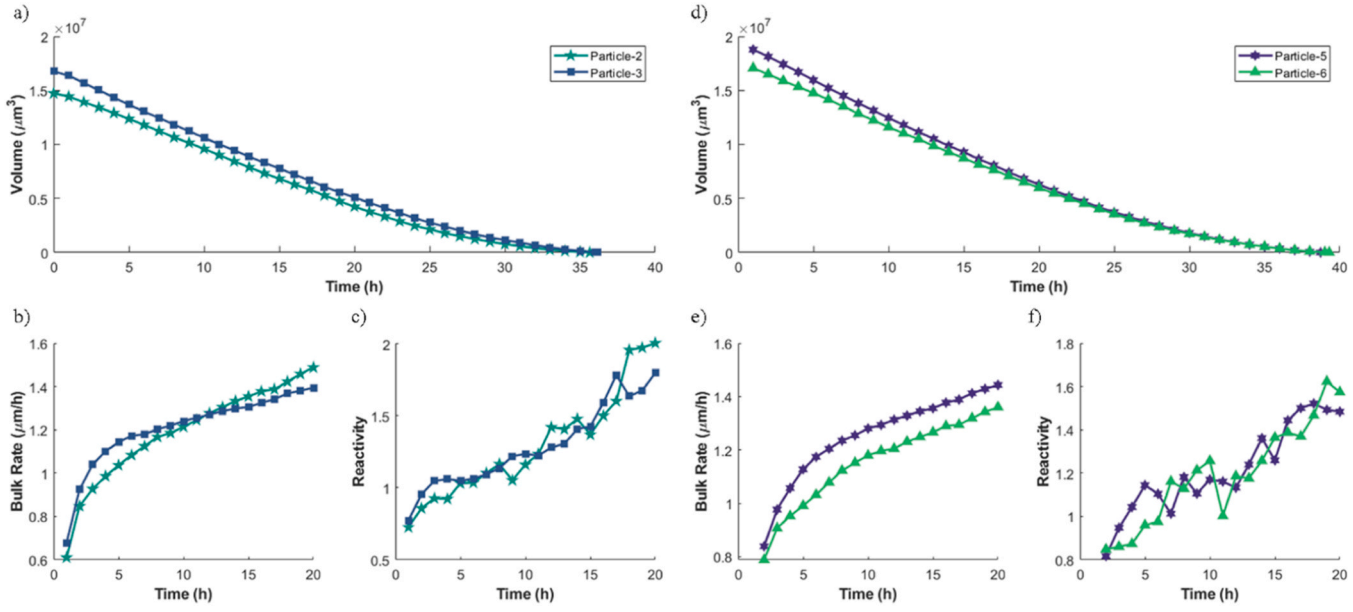

Fig. 5. Time resolved results from the empirical dissolution model applied to galena particle-2 and particle-3 (a-c), and particle-5 and particle-6 (d-f). Each data point refers to the result after each hour of simulated dissolution, thus after 1000 iterations of the model.

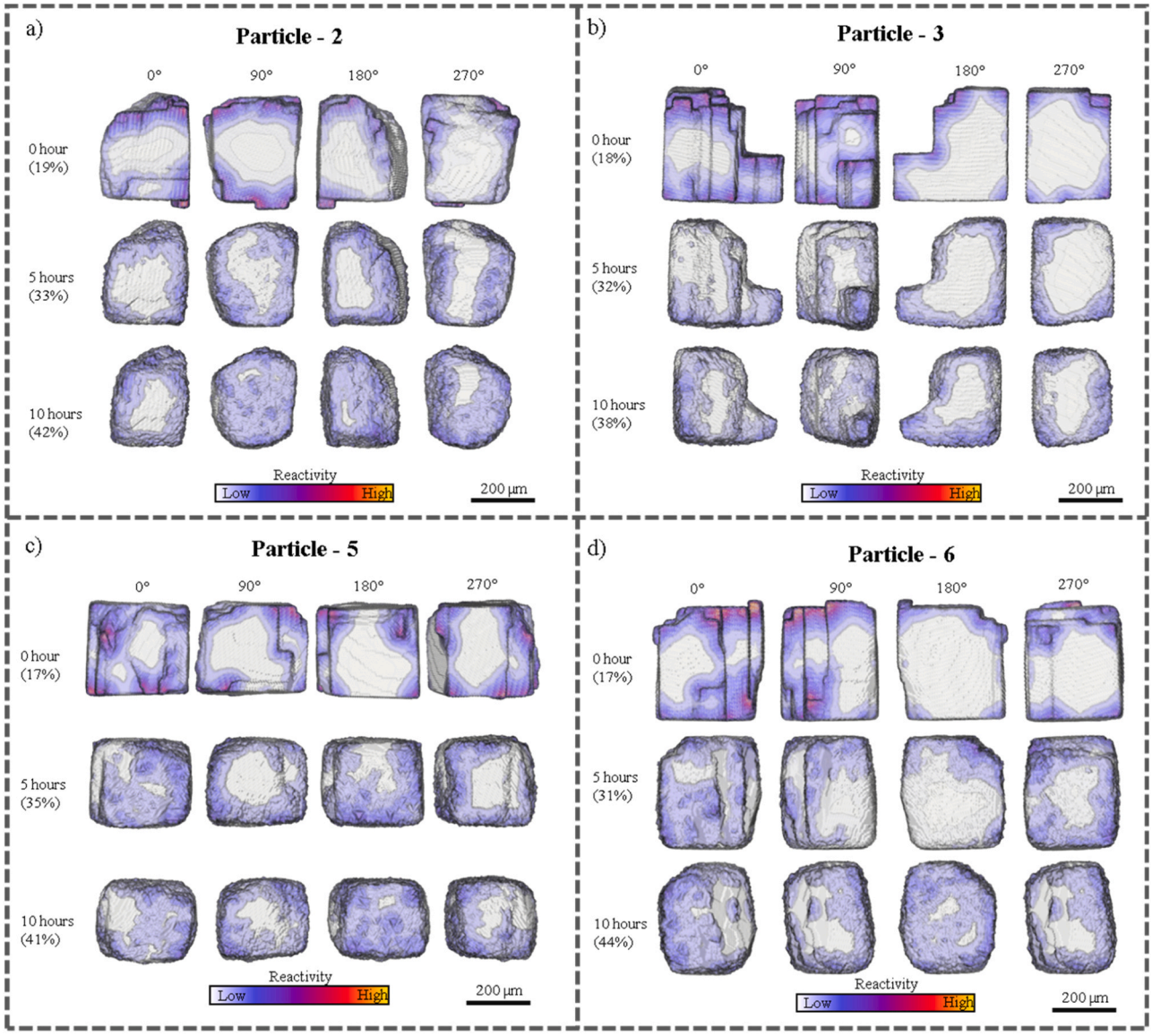

Fig. 6. Visualization of the empirical dissolution model results illustrating morphology, size and reactivity along with the calculated Features to Surface Percentage (FSP) values of (a) particle-2, (b) particle-3, (c) particle-5 and (d) particle-6 at 0 h (i.e. prior to dissolution), 5 h and 10 h dissolution time. Each particle is shown in different positions (0°, 90°, 180° and 360°). Note that the reactivity color bars were adjusted to facilitate comparison and highlight the reactivity variations over time.

global bulk dissolution rate and normalized global bulk dissolution rate of 5.94 µm.h^{-1} and 5.1×10^{-5} mol.m^{-2}.s^{-1}, respectively. The somewhat higher global bulk dissolution rate obtained by Jenkin et al. [21] is tentatively attributed to surface polishing, which is known to enhance the dissolution, especially during early stages [43]. Furthermore, the surface orientation of the galena was not mentioned, which likely makes it more reactive compared to the {001} terraces of the galena surface within this study [13]. Nonetheless, the normalized bulk dissolution rate reported by Jenkin et al. [21] is within the same order of magnitude as the one reported in this study, demonstrating that the model presented here is still within an adequate range.

Atomic dissolution models such as the kinetic Monte-Carlo (kMC) simulation [19,26,39] utilize a stochastic or probability-based approach to simulate the detachment of atoms from a mineral surface. kMC models can predict the dissolution behavior of a mineral surface but only on limited fields of view due to the intensive computational power required to upscale the model, e.g. simulate the dissolution of many particles. On the other hand, the proposed empirical dissolution model was derived from the correlation between the experimental dissolution rates spectra and the distance between macroscopic features and surface points. The probability of atom detachment was assumed to be accounted for in the experimental result dissolution rates spectra. As shown in Fig. 3c, the experimental result of the galena-x particle captures the higher dissolution rates at corners and edges similar to the higher probability of dissolution at the analogous feature on atomic-scale. Even though the resolution of the 3D images used in this work is insufficient to resolve the dissolution processes on terraces, it effectively captures the significantly higher reactivity at corners and edges. This suggests that considering the nearly atomic-flat planes of minerals that are typically studied experimentally and numerically is not sufficient to predict dissolution at the particle level. Nevertheless, the model proposed here is compatible with those previous studies, e.g. the step wave model [28]. For example, steps and corners can be seen as permanent sources of instability from where continuous waves of steps are emanated in all directions, thus justifying the macroscale correlations found of reactivity vs distance from the feature.

Furthermore, the empirical dissolution model can be simply achieved by calculating the distance between the feature points and surface

points along any crystal direction. Therefore, single particle leaching experiments using other minerals can be used to simulate the changes in geometry during dissolution even in other solutions (e.g. aqueous), assuming that the experimental variables affecting the dissolution rate would remain constant and that there are no interactions between particles throughout the dissolution process. Despite the limitations, the empirical dissolution model can simulate multiple mineral particle dissolution with less computational power, as shown by the computing time needed to simulate the dissolution of galena-x particle and the seven galena particles, which present the advantages of the model over atomic-scale models. However, computing power will increase proportionally with the total number of voxels that need to be simulated.

Yet, the empirical dissolution model can be optimized even further. Firstly, the kernel utilized to calculate the Gaussian curvature plays an essential role in detecting the macroscopic features within the particle surface. The kernel size can be optimized according to the macroscopic feature size. The application of a kernel size smaller than the one used here resulted in the identification of more surface features but was found also to create artifacts, such as staircase morphologies within otherwise flat surfaces. Using larger kernel sizes decreased lateral resolution, resulting in multiple distinct macroscopic features merging and fewer detected surface features. This will affect the correlation between the calculated distance map and the dissolution rate spectra. On the contrary, larger kernel size decreased lateral resolution, resulting in multiple distinct macroscopic features merging and fewer detected surface features. In this study, a 3x3x3 kernel was utilized, which within some parts of the galena-x particle can be seen to distinguish the macroscopic corners within the plane intersection (corners and edges) yet had difficulties distinguishing features on terraces. This was apparent within Fig. 3d, highlighted by the yellow arrow, which displays the high reactivity within the steps of the galena-x terraces. This, in turn, will affect the correlation between the calculated distance map and the dissolution rates spectra, resulting in a higher reactivity and discrepancy between calculated global bulk dissolution rate and simulated result. However, the optimization of the kernel size can be done by using adaptive kernel algorithms such as features from accelerated segment test (FAST, [40]), which utilizes machine learning for feature detection.

Secondly, the dissolution rates spectra were determined by measuring the surface retreat of the dissolving particle using chamfer distance. Chamfer distance calculated the Euclidean distance perpendicular to the surface of the particle towards the internal part of the particle. However, dissolution occurred not only perpendicular to the surface but also along the terraces (parallel to the surface), resulting in higher uncertainties in the calculation of dissolution rates spectra within terraces. Other sources of uncertainties may include the calculation of the reactivity map, as it is derived from the correlation between dissolution rates spectra and the distance between surface features and surface points. Complimentary techniques using synchrotron radiation, for example, would be beneficial to further improve the empirical dissolution model, especially to unravel the dissolution within terraces.

On the application to the seven galena particles, the applied empirical dissolution model highlights the importance of initial particle geometries in investigating mineral dissolution. The model successfully captured both volume and reactivity changes of the seven galena particles. The rounding of the surface and the increased roughness within the surface morphology are also evident (Fig. 6). This evolution in surface morphology increases the amount of surface area considered as macroscopic features by the model, thus leading to a gradual increase of average reactivity over time (Fig. 5). This was demonstrated by the comparison between particle-2 to particle-3 and particle-5 to particle-6. Particle-3 exhibits higher initial average reactivity, although the amount of FSP was lower than particle-2. This could originate from the position of the macroscopic features within particle-3 (Fig. 6b), in which macroscopic features are in close proximity to one another. Therefore, displays significant reactivity, especially prior to dissolution at viewing angles of 0° and 90°. This corresponds to the observation of [49] which shows that the reactivity of a surface is also affected not only by the closest macroscopic features but also by the presence of other distant macroscopic features. Thus, leads to higher reactivity in comparison to particle-2. On the other hand, particle-6 required 1 hour longer to dissolve in comparison to particle-5 despite having a smaller volume. The reason could originate from the fact that the roughness of the particle surface increases during the dissolution process, which was evident in particle-5 (Fig. 6c). The surface roughness increases the macroscopic features over the surface resulting in an increase in reactivity. This is because as the particle shrinks, every point of the surface is closer to the macroscopic features. Consequently, our work suggests that in a system of particles being dissolved in a batch reactor, the overall dissolution rate is expected to increase over time due to the changes of particle morphology, by which smaller particles imply higher surface reactivity. Additionally, extrapolating the observations to industrial leaching of minerals, the results suggest that the leaching rate will not only depend on the particle size, but also of the comminution method use, which can affect the initial morphology of particle and the amount of features exposed.

5. Conclusion

This study utilizes X-ray computed tomography (CT) to address the challenges associated with understanding mineral dissolution processes. The identification of macroscopic features using surface curvatures and the calculation of the reactivity map can be utilized to upscale mineral dissolution simulation, particularly towards the macroscopic scale (μm-mm scale). The proposed empirical model for monomineralic galena particle dissolving in an ethaline solution effectively utilizes the close link between dissolution rates spectra as determined experimentally and the initial particle three-dimensional geometry described by surface curvature calculations. The case study of galena-x particle highlights the importance of considering the mineral macroscopic features during the dissolution process, as shown by the rapid dissolution captures within these features. Furthermore, this finding suggests that it is insufficient to rely solely on investigation of the nearly atomic-flat planes of minerals to predict dissolution at the particle level; instead, a complementary examination of the particle three-dimensional geometry is necessary.

The application of the empirical dissolution model to the seven galena particles demonstrates that the proposed model can be successfully applied to mineral particles with various shapes and sizes, which allows the monitoring of the particle volume, geometry and reactivity evolution throughout the dissolution process. The simulation results display an increasing amount of surface reactivity as a consequence of the geometry progression. Thus, further emphasizes the importance of particle geometry evolution in determining the mineral dissolution behavior and dissolution rates. Furthermore, the difference in reactivity due to geometry highlights that normalizing the dissolution rate to the overall surface area, without accounting for the effect of macroscopic features, may not represent the actual reactivity of the dissolving particles, leading to a discrepancy in the global bulk dissolution rates.

Funding

This work was part of the ION4RAW project that received funding from the European Union's EU Framework Programme for Research and Innovation Horizon 2020 under under Grant Agreement No 815748.

CRediT authorship contribution statement

Chandra Widyananda Winardhi: Writing – original draft, Validation, Software, Methodology, Formal analysis, Conceptualization. **Jens Gutzmer:** Writing – review & editing, Supervision. **Veerle Cnudde:** Writing – review & editing, Supervision. **Jose Ricardo da Assuncao Godinho:** Writing – review & editing, Methodology, Conceptualization.

Declaration of Competing Interest

The authors declare that they have no known competing financial interests or personal relationships that could have appeared to influence the work reported in this paper.

Acknowledgements

The authors gratefully acknowledge the Geoscientific Collections of the TU Bergakademie Freiberg for providing the galena particles sample and Camila Guimarães da Silva Tochtrop for the help preparing the seven galena particles sample.

Appendix A

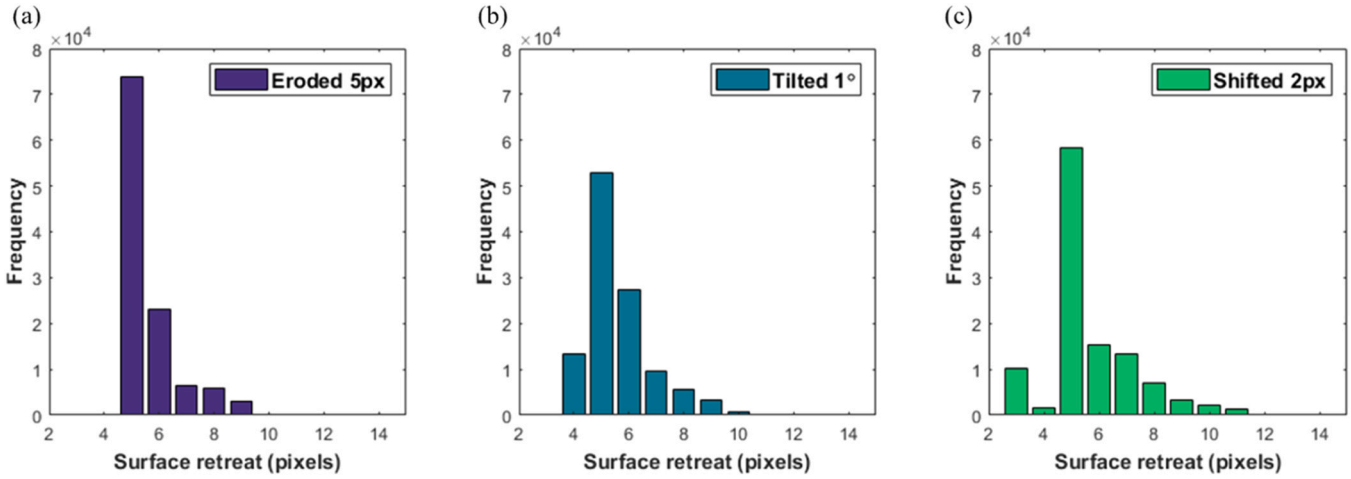

Figure A.1. Surface retreat distribution of possible uncertainty due to misregistration, (a) the new volume with 5-pixel 3D erosion, (b) 1° vertical angle tilting and (c) 2-pixel horizontal shift.

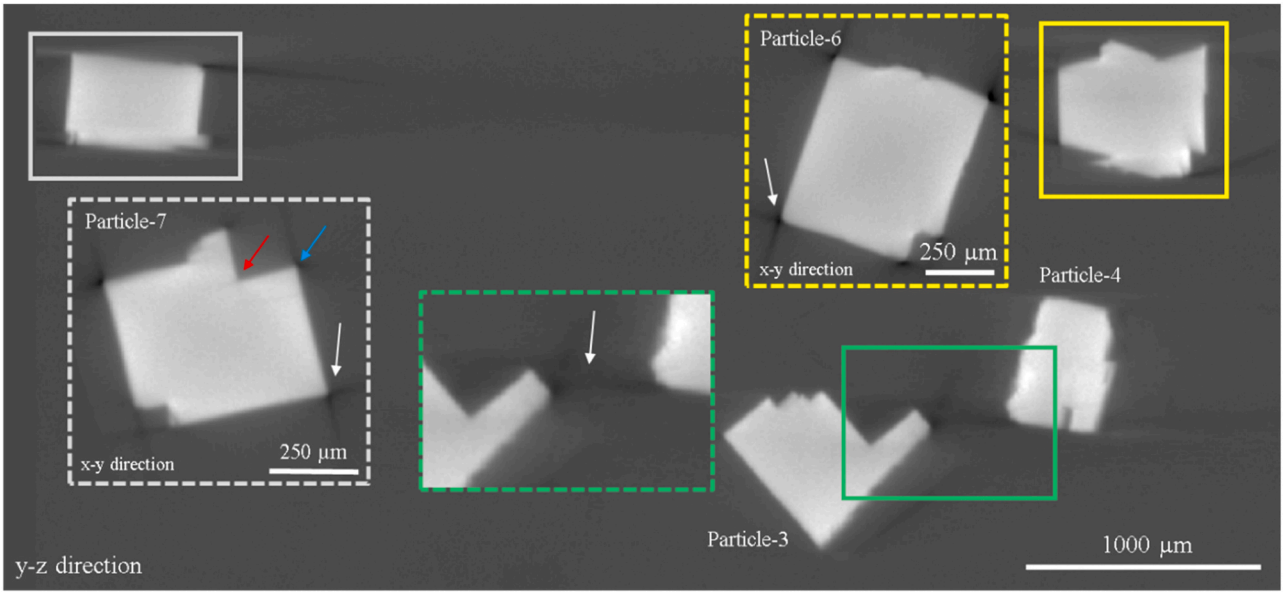

Figure A.2. Ortho-slice visualization in y-z direction of particle 3, 4, 6 and 7 prior to image processing. White arrows indicate artifact caused by the sharp corners or the particles. The red and blue arrows show the inward-facing features (i.e. re-entrant corners or edges) the outward-facing features (i.e. convex corners or edges) respectively. Note the dotted green square highlighting the artifact between two nearby particles.

References

[1] A.P. Abbott, A.Z.M. Al-Bassam, A. Goddard, R.C. Harris, G.R.T. Jenkin, F.J. Nisbet, M. Wieland, Dissolution of pyrite and other Fe–S–as minerals using deep eutectic solvents, Green. Chem. 19 (9) (2017) 2225–2233, https://doi.org/10.1039/C7GC00334J.

[2] P. Agrawal, A. Mascini, T. Bultreys, H. Aslannejad, M. Wolthers, V. Cnudde, I. B. Butler, A. Raoof, The impact of pore-throat shape evolution during dissolution on carbonate rock permeability: pore network modeling and experiments, Adv. Water Resour. 155 (2021) 103991, https://doi.org/10.1016/j.advwatres.2021.103991.

[3] M. Akmal Butt, P. Maragos, Optimum design of chamfer distance transforms, IEEE Trans. Image Process. 7 (10) (1998) 1477–1484, https://doi.org/10.1109/83.718487.

[4] R.S. Arvidson, I.E. Ertan, J.E. Amonette, A. Luttge, Variation in calcite dissolution rates, Geochim. Cosmochim. Acta 67 (9) (2003) 1623–1634, https://doi.org/10.1016/S0016-7037(02)01177-8.

[5] A.H. Bentbib, M. El Guide, K. Jbilou, L. Reichel, A global Lanczos method for image restoration, J. Comput. Appl. Math. 300 (2016) 233–244, https://doi.org/10.1016/j.cam.2015.12.034.

[6] E. Bidari, C.W. Winardhi, J.R. da A. Godinho, G. Frisch, Role of oxidants in metal extraction from sulfide minerals in a deep eutectic solvent, ACS Omega (2024), https://doi.org/10.1021/acsomega.4c01052.

[7] V. Cnudde, M.N. Boone, High-resolution X-ray computed tomography in geosciences: a review of the current technology and applications, Earth-Sci. Rev. 123 (2013) 1–17, https://doi.org/10.1016/j.earscirev.2013.04.003.

[8] G.K.W. Dawson, J.K. Pearce, D. Biddle, S.D. Golding, Experimental mineral dissolution in Berea Sandstone reacted with CO2 or SO2–CO2 in NaCl brine under CO2 sequestration conditions, Chem. Geol. 399 (2015) 87–97, https://doi.org/10.1016/j.chemgeo.2014.10.005.

[9] C. Fischer, R.S. Arvidson, A. Lüttge, How predictable are dissolution rates of crystalline material? Geochim. Et. Cosmochim. Acta 98 (2012) 177–185, https://doi.org/10.1016/j.gca.2012.09.011.

[10] E.S.L. Gastal, M.M. Oliveira, Adaptive manifolds for real-time high-dimensional filtering, ACM Trans. Graph. 31 (4) (2012) 1–13, https://doi.org/10.1145/2185520.2185529.

[11] L. George, N.J. Cook, L. Cristiana, C, Wade, B. P, Trace and minor elements in galena: a reconnaissance LA-ICP-MS study, Am. Mineral. 100 (2-3) (2015) 548–569, https://doi.org/10.2138/am-2015-4862.

[12] Y. Ghorbani, J. Petersen, M. Becker, A.N. Mainza, J.P. Franzidis, Investigation and modelling of the progression of zinc leaching from large sphalerite ore particles, Hydrometallurgy 131 (2013) 8–23, https://doi.org/10.1016/j.hydromet.2012.10.004.

[13] J.R.A. Godinho, S. Piazolo, T. Balic-Zunic, Importance of surface structure on dissolution of fluorite: Implications for surface dynamics and dissolution rates, Geochim. Et. Cosmochim. Acta 126 (2014) 398–410, https://doi.org/10.1016/j.gca.2013.11.017.

[14] J.R.A. Godinho, A.G. Stack, Growth kinetics and morphology of barite crystals derived from face-specific growth rates, Cryst. Growth Des. 15 (5) (2015) 2064–2071, https://doi.org/10.1021/cg501507p.

[15] J.R.A. Godinho, B.L.D. Grilo, F. Hellmuth, A. Siddique, Mounted single particle characterization for 3D mineralogical analysis—MSPaCMAn, Article 9. Minerals 11 (9) (2021) https://doi.org/10.3390/min11090947.

[16] M.G. Guren, F. Renard, C. Noiriel, Dissolution rate variability at carbonate surfaces: 4D X-ray micro-tomography and stochastic modeling investigations, Front. Water 5 (2023), https://doi.org/10.3389/frwa.2023.1185608.

[17] G.R. Holdren, P.M. Speyer, Reaction rate-surface area relationships during the early stages of weathering—I. Initial observations, Geochim. Cosmochim. Acta 49 (3) (1985) 675–681, https://doi.org/10.1016/0016-7037(85)90162-0.

[18] A.B.M.R. Islam, J.P. Maity, J. Bundschuh, C.-Y. Chen, B.K. Bhowmik, K. Tazaki, Arsenic mineral dissolution and possible mobilization in mineral–microbe–groundwater environment, J. Hazard. Mater. 262 (2013) 989–996, https://doi.org/10.1016/j.jhazmat.2012.07.022.

[19] M. Izadifar, N. Ukrainczyk, K.M. Salah Uddin, B. Middendorf, E. Koenders, Dissolution of β-C2S cement clinker: part 2 atomistic kinetic Monte Carlo (KMC) upscaling approach, Materials 15 (19) (2022) 6716, https://doi.org/10.3390/ma15196716.

[20] Z. Jangda, H. Menke, A. Busch, S. Geiger, T. Bultreys, H. Lewis, K. Singh, Pore-scale visualization of hydrogen storage in a sandstone at subsurface pressure and temperature conditions: trapping, dissolution and wettability, J. Colloid Interface Sci. 629 (2023) 316–325, https://doi.org/10.1016/j.jcis.2022.09.082.

[21] G.R.T. Jenkin, A.Z.M. Al-Bassam, R.C. Harris, A.P. Abbott, D.J. Smith, D. A. Holwell, R.J. Chapman, C.J. Stanley, The application of deep eutectic solvent ionic liquids for environmentally-friendly dissolution and recovery of precious metals, Miner. Eng. 87 (2016) 18–24, https://doi.org/10.1016/j.mineng.2015.09.026.

[22] W.-A. Kahl, T. Yuan, T. Bollermann, W. Bach, C. Fischer, Crystal surface reactivity analysis using a combined approach of X-ray micro-computed tomography and vertical scanning interferometry, Am. J. Sci. 320 (1) (2020) 27–52, https://doi.org/10.2475/01.2020.03.

[23] S. Khandelwal, Y.K. Tailor, M. Kumar, Deep eutectic solvents (DESs) as eco-friendly and sustainable solvent/catalyst systems in organic transformations, J. Mol. Liq. 215 (2016) 345–386, https://doi.org/10.1016/j.molliq.2015.12.015.

[24] J.J. Koenderink, A.J. van Doorn, Surface shape and curvature scales, Image Vis. Comput. 10 (8) (1992) 557–564, https://doi.org/10.1016/0262-8856(92)90076-F.

[25] I. Kurganskaya, A. Luttge, Mineral dissolution kinetics: pathways to equilibrium, ACS Earth Space Chem. 5 (7) (2021) 1657–1673, https://doi.org/10.1021/acsearthspacechem.1c00017.

[26] I. Kurganskaya, N. Trofimov, A. Luttge, A Kinetic Monte Carlo approach to model barite dissolution: the role of reactive site geometry, Minerals 12 (5) (2022) 639, https://doi.org/10.3390/min12050639.

[27] I. Kurganskaya, R.D. Rohlfs, A. Luttge, Multi-scale modeling of crystal-fluid interactions: State-of-the-art, challenges and prospects. In Reference Module in Chemistry, Molecular Sciences and Chemical Engineering, Elsevier, 2023, https://doi.org/10.1016/B978-0-323-85669-0.00034-9.

[28] A.C. Lasaga, A. Luttge, Variation of crystal dissolution rate based on a dissolution stepwave model, Science 291 (5512) (2001) 2400–2404, https://doi.org/10.1126/science.1058173.

[29] A. Lüttge, R.S. Arvidson, C. Fischer, Fundamental controls of dissolution rate spectra: comparisons of model and experimental results, Procedia Earth Planet. Sci. 7 (2013) 537–540, https://doi.org/10.1016/j.proeps.2013.03.115.

[30] Q. Lin, D.J. Barker, K.J. Dobson, P.D. Lee, S.J. Neethling, Modelling particle scale leach kinetics based on X-ray computed micro-tomography images, Hydrometallurgy 162 (2016) 25–36, https://doi.org/10.1016/j.hydromet.2016.02.008.

[31] P. Martin, J.J. Gaitero, J.S. Dolado, H. Manzano, New kinetic Monte Carlo model to study the dissolution of quartz, ACS Earth Space Chem. 5 (3) (2021) 516–524, https://doi.org/10.1021/acsearthspacechem.0c00303.

[32] J. Milot, J. Blichert-Toft, M.A. Sanz, C. Malod-Dognin, P. Télouk, F. Albarède, Silver isotope and volatile trace element systematics in galena samples from the Iberian Peninsula and the quest for silver sources of Roman coinage, Geology 50 (4) (2022) 422–426, https://doi.org/10.1130/G49690.1.

[33] F. Montserrat, P. Renforth, J. Hartmann, M. Leermakers, P. Knops, F.J.R. Meysman, Olivine Dissolution in Seawater: Implications for CO2 Sequestration through Enhanced Weathering in Coastal Environments, Environ. Sci. Technol. 51 (7) (2017) 3960–3972, https://doi.org/10.1021/acs.est.6b05942.

[34] C. Muzawazi, J. Petersen, Heap and tank leaching of copper and nickel from a Platreef flotation concentrate using ammoniacal solutions, Can. Metall. Q. 54 (3) (2015) 297–304, https://doi.org/10.1179/1879139515Y.0000000017.

[35] C. Noiriel, L. Luquot, B. Madé, L. Raimbault, P. Gouze, J. Van Der Lee, Changes in reactive surface area during limestone dissolution: an experimental and modelling study, Chem. Geol. 265 (1–2) (2009) 160–170, https://doi.org/10.1016/j.chemgeo.2009.01.032.

[36] C. Noiriel, M. Oursin, D. Daval, Examination of crystal dissolution in 3D: a way to reconcile dissolution rates in the laboratory? Geochim. Et. Cosmochim. Acta 273 (2020) 1–25, https://doi.org/10.1016/j.gca.2020.01.003.

[37] F.M. Perna, P. Vitale, V. Capriati, Deep eutectic solvents and their applications as green solvents, Curr. Opin. Green. Sustain. Chem. 21 (2020) 27–33, https://doi.org/10.1016/j.cogsc.2019.09.004.

[38] K. Radošević, M. Cvjetko Bubalo, V. Gaurina Srček, D. Grgas, T. Landeka Dragičević, I. Radojčić Redovniković, Evaluation of toxicity and biodegradability of choline chloride based deep eutectic solvents, Ecotoxicol. Environ. Saf. 112 (2015) 46–53, https://doi.org/10.1016/j.ecoenv.2014.09.034.

[39] R.D. Rohlfs, C. Fischer, I. Kurganskaya, A. Luttge, Crystal dissolution kinetics studied by a combination of Monte Carlo and Voronoi methods, Minerals 8 (4) (2018) 133, https://doi.org/10.3390/min8040133.

[40] Rosten, E., & Drummond, T. (2006). Machine learning for high-speed corner detection. In Computer Vision–ECCV 2006: 9th European Conference on Computer Vision, Graz, Austria, May 7-13, 2006. Proceedings, Part I 9 (pp. 430-443). Springer Berlin Heidelberg. https://doi.org/10.1007/11744023_34.

[41] E. Ruiz-Agudo, C.V. Putnis, C. Jiménez-López, C. Rodriguez-Navarro, An atomic force microscopy study of calcite dissolution in saline solutions: the role of magnesium ions, Geochim. Et. Cosmochim. Acta 73 (11) (2009) 3201–3217, https://doi.org/10.1016/j.gca.2009.03.016.

[42] Russ, J.C. (2006). The Image Processing Handbook (0 ed.). CRC Press. https://doi.org/10.1201/9780203881095.

[43] G.D. Saldi, M. Voltolini, K.G. Knauss, Effects of surface orientation, fluid chemistry and mechanical polishing on the variability of dolomite dissolution rates, Geochim. Et. Cosmochim. Acta 206 (2017) 94–111, https://doi.org/10.1016/j.gca.2017.02.007.

[44] V. Saxena, S. Ahmed, Dissolution of fluoride in groundwater: A water-rock interaction study, Environ. Geol. 40 (9) (2001) 1084–1087, https://doi.org/10.1007/s002540100290.

[45] B. Schulz, G. Merker, J. Gutzmer, Automated SEM Mineral Liberation Analysis (MLA) with Generically Labelled EDX Spectra in the Mineral Processing of Rare Earth Element Ores, Minerals 9 (9) (2019) 527, https://doi.org/10.3390/min9090527.

[46] S. Spathariotis, N. Peeters, S. Ryder, K, P. Abbott, A, K. Binnemans, S. Riaño, 2020, Separation of iron(iii), zinc(ii) and lead(ii) from a choline chloride–ethylene glycol deep eutectic solvent by solvent extraction. RSC Advances, 10(55), 33161–33170. https://doi.org/10.1039/D0RA06091G.

[47] C. Studholme, D.L.G. Hill, D.J. Hawkes, An overlap invariant entropy measure of 3D medical image alignment, Pattern Recognit. 32 (1) (1999) 71–86, https://doi.org/10.1016/S0031-3203(98)00091-0.

[48] A.V. Subhas, N.E. Rollins, W.M. Berelson, S. Dong, J. Erez, J.F. Adkins, A novel determination of calcite dissolution kinetics in seawater, Geochim. Cosmochim. Acta 170 (2015) 51–68, https://doi.org/10.1016/j.gca.2015.08.011.

[49] C.W. Winardhi, J.R.A. Godinho, J. Gutzmer, The Effect of Macroscopic Particle Features on Mineral Dissolution, Article 2. Minerals 13 (2) (2023) https://doi.org/10.3390/min13020253.

[50] C.W. Winardhi, J.R.A. Godinho, C. Rachmawati, I.D. Achin, A.U. Iturbe, G. Frisch, J. Gutzmer, A particle-based approach to predict the success and selectivity of leaching processes using ethaline—comparison of simulated and experimental results, Hydrometallurgy 211 (2022) 105869, https://doi.org/10.1016/j.hydromet.2022.105869.

[51] P.J. Withers, C. Bouman, S. Carmignato, V. Cnudde, D. Grimaldi, C.K. Hagen, E. Maire, M. Manley, A. Du Plessis, S.R. Stock, X-ray computed tomography, Nat. Rev. Methods Prim. 1 (1) (2021) 18, https://doi.org/10.1038/s43586-021-00015-4.

[52] S. Yagi, D. Kunii, Studies on combustion of carbon particles in flames and fluidized beds, Symp. . (Int.) Combust. 5 (1) (1955) 231–244, https://doi.org/10.1016/S0082-0784(55)80033-1.

[53] K. Yuan, V. Starchenko, S.S. Lee, V. De Andrade, D. Gursoy, N.C. Sturchio, P. Fenter, Mapping three-dimensional dissolution rates of calcite microcrystals: effects of surface curvature and dissolved metal ions, ACS Earth Space Chem. 3 (5) (2019) 833–843, https://doi.org/10.1021/acsearthspacechem.9b00003.

[54] J. Zheng, Q. Sun, H. Zheng, D. Wei, Z. Li, L. Gao, Three-dimensional particle shape characterizations from half particle geometries, Powder Technol. 367 (2020) 122–132, https://doi.org/10.1016/j.powtec.2020.03.046.